Smart Structures and Systems, *Vol. 29, No. 2 (2022) 267-278*
https://doi.org/10.12989/sss.2022.29.2.267

Bending characteristics of Prestressed High Strength Concrete (PHC) spun pile measured using distributed optical fibre strain sensor

Hisham Mohamad*[1], Bun Pin Tee [2,3], Mun Fai Chong [4], Siew Cheng Lee [2] and Krisada Chaiyasarn [5]

[1] *Civil & Environmental Engineering Department, Universiti Teknologi PETRONAS, 32610 Seri Iskandar, Perak, Malaysia*
[2] *Smart Sensing Technology Sdn. Bhd., 40150 Shah Alam, Selangor, Malaysia*
[3] *School of Civil Engineering, Universiti Teknologi Malaysia, 81310 Skudai, Johor, Malaysia*
[4] *Dynamic Pile Testing Sdn. Bhd., 40150 Shah Alam, Selangor, Malaysia*
[5] *Thammasat School of Engineering, Thammasat University Rangsit, Klong Luang Pathumthani, Thailand*

(*Received April 12, 2020, Revised February 22, 2021, Accepted September 18, 2021*)

Abstract. Pre-stressed concrete circular spun piles are widely used in various infrastructure projects around the world and offer an economical deep foundation system with consistent and superior quality compared to cast in-situ and other concrete piles. Conventional methods for measuring the lateral response of piles have been limited to conventional instrumentation, such as electrical based gauges and pressure transducers. The problem with existing technology is that the sensors are not able to assist in recording the lateral stiffness changes of the pile which varies along the length depending on the distribution of the flexural moments and appearance of tensile cracks. This paper describes a full-scale bending test of a 1-m diameter spun pile of 30 m long and instrumented using advanced fibre optic distributed sensor, known as Brillouin Optical Time Domain Analysis (BOTDA). Optical fibre sensors were embedded inside the concrete during the manufacturing stage and attached on the concrete surface in order to measure the pile's full-length flexural behaviour under the prescribed serviceability and ultimate limit state. The relationship between moments-deflections and bending moments-curvatures are examined with respect to the lateral forces. Tensile cracks were measured and compared with the peak strains observed from BOTDA data which corroborated very well. By analysing the moment-curvature response of the pile, the structure can be represented by two bending stiffness parameters, namely the pre-yield (EI) and post-yield (EI_{cr}), where the cracks reduce the stiffness property by 89%. The pile deflection profile can be attained from optical fibre data through closed-form solutions, which generally matched with the displacements recorded by Linear Voltage Displacement Transducers (LVDTs).

Keywords: BOTDA; bending stiffness; moment-curvature; prestressed high strength concrete; spun pile; tensile cracks

1. Introduction

Pile foundations are often required to support tall buildings and heavy infrastructures by transferring loads to a deeper and competent soil layer. The common types of piles include cast in-situ piles (large-diameter bored piles, barrettes, and micropiles) and precast piles or driven piles (concrete piles and steel H-piles). Precast piles such as spun-cast concrete tubular piles, are manufactured by spinning wet concrete in a formwork with pre-tensioned wires installed, typically known as prestressed high strength concrete (PHC) spun-cast piles. The cylinder pile sections are spun centrifugally during the casting process, causing the concrete to compact while forcibly removing water during the curing resulting in a high density, durable concrete that is virtually impervious to moisture (Whiting 1952, Völgyi *et al*. 2010). The pretension adds tensile strength to the pile. Depending on the manufacturer, the compressive strength of the concrete and the tensile strength of the pre-tensioned wires are approximately 80 MPa and 1,420 MPa, respectively. The outer diameter of the pile varies from 300 mm to 1200 mm and wall thicknesses of 60 mm to 150 mm are available depending on the pile diameter. The design load-carrying capacity of the pile ranges from 900 kN to 9000 kN with precast lengths of 12 m to 30 m.

PHC spun piles were originally developed for marine structures in the 1950s for structures that required high axial load resistance, high bending stiffness and, most importantly, high resistance to corrosion (Hartman *et al*. 2007). With their high bending strength-to-weight ratio, spun-cast piles offer a significant advantage for piles with long unsupported lengths. Verification of structural performance and serviceability of spun-cast piles are widely available in the literature (e.g., Rausche and Webster 2007, Chow and Tan 2010, Abu-Farsakh *et al*. 2017). Although the spun-cast piles are manufactured to the specified high tensile strength, tensile cracks may occur before and during installation (i.e., transportation and driving stages) and after installation such as service loads (Avent and Mukai 1998). Others reported issues include ground movement (Liew *et al*. 2010, Hong *et al*. 2019), large access pore water pressure (Ni *et al*. 2017), in addition to prestressing strands which may deteriorate due to long-term exposure of moisture (Aso *et al*. 2004, Abendroth *et al*. 2007).

*Corresponding author, Ph.D., P.E., Associate Professor,
E-mail: hisham.mohamad@utp.edu.my

ISSN: 1738-1584 (Print), 1738-1991 (Online)

Distributed Optical Fibre Strain Sensor (DOFSS) has the advantage of detecting cracks at any arbitrary location along the structure and at the same time measures the pile's deformation profile, such as curvature and displacement (e.g., Goldfeld and Klar 2013, Mohamad *et al*. 2019). This research presents the first full-scale bending test of large diameter (1 m dia.) and very long length (30 m) spun piles using optical fibre strain sensors together with a variety of displacement gauges. Optical fibre sensors were fully embedded inside the concrete and fully attached along the pile's surface in order to measure curvature changes and investigate the development of tensile cracks at several stages of bending loads.

2. Distributed Optical Fibre Strain Sensor (DOFSS)

Distributed fibre optic strain sensing is one of the many types of optical fibre technology that have been increasingly applied in geotechnical fields, such as piled foundations, retaining walls, pipelines, tunnels and pavements (Feng *et al*. 2015, Bao *et al*. 2016, Huang *et al*. 2017, Pelecanos *et al*. 2018). The novelty of this technology is that a single optical fibre can sense over its full length of the cable (replacing thousands of point-wise strain gauges - potentially up to 50 km long) and detect any strain and temperature changes. The advantages of distributed fibre optic sensors include geometrical adaptability, dual task of sensor and path for transmission of the signal, precision and sensitivity over large measurement ranges, and immunity to electromagnetic interference and electrical hazard (Kesavan *et al*. 2005, Liu *et al*. 2017). In pile design, measuring continuous strain profile is important in determining the load-transfer mechanism of the foundation through embedding optical cables in cast in-situ piles (Pelecanos *et al*. 2018, Mohamad *et al*. 2017) or by surface adhesion of precast piles (Lu *et al*. 2012).

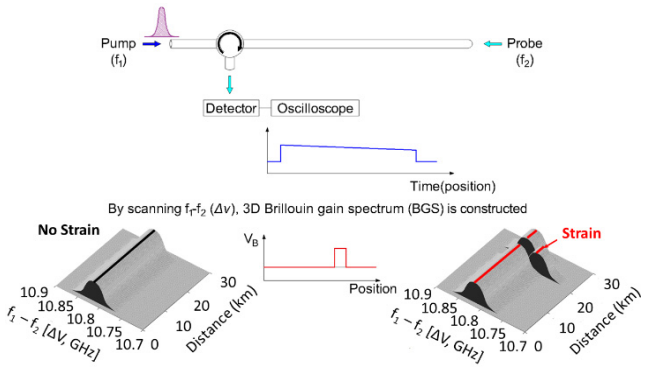

Fig. 1 Principle of BOTDA sensor system

2.1 Principle of Brillouin Optical Time Domain Analysis (BOTDA)

BOTDA supply continuous distributed strain measurements by utilising the backward stimulated Brillouin scattering of an optical fibre (Huang *et al*. 2017). The pumping pulse light is launched at one end of the fibre and propagates in the fibre, while the continuous wave (CW) light is launched at the opposite end of the fibre and propagates in the opposite direction, as shown in Fig. 1. In this configuration, the pump pulse generates backward Brillouin gain in a single-mode fibre. When the frequency difference between CW signal and pump pulse is equal to Brillouin frequency of the optical fibre, the two counter-propagating signals interact, leading to a larger scattering efficiency and an amplification of the probe signal. Also, the Brillouin frequency of a fibre is changed by the strain or temperature applied on the fibre. In this study, a BOTDA analyser manufactured by OZ Optics Ltd. is adopted with reported strain accuracy ($2s$) of $\pm 2\ \mu\varepsilon$ (Zou *et al*. 2006).

2.2 Fibre optic cables

Fig. 2 shows the configuration of a 5.0 mm diameter optical cable specifically designed by NanZee for embedment in concrete piles (Mohamad *et al*. 2016, 2017). It consists of a single core single mode fibre reinforced with six strands of steel wires and polyethylene cable jacket. The external plastic coating and the inner glass core are fixed together so that the strain applied externally (from the concrete) is fully transferred from the coating to the inner

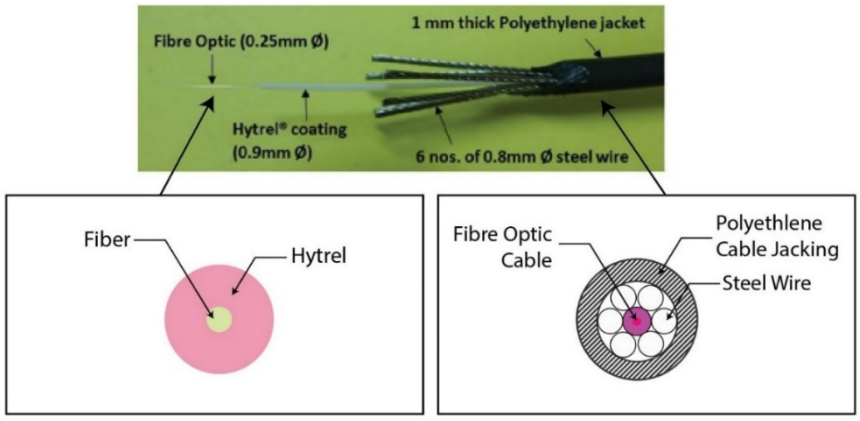

(a) The inner fibre (b) The overall configuration of reinforced steel wired cable

Fig. 2 Reinforced strain sensing cable (top figure) with cross-sectional views. The inner fibre can also be configured as surface mounted cable

Table 1 Specification of PHC spun pile used in this study with concrete grade 80 N/mm^2

External diameter (mm)	Wall thickness (mm)	Length (m)	Weight (kg/m)	No. of pre-stressing strand (12.6 mm)	Bending moment capacity, M_{cr} (kNm)	Recommended max axial working load (for a short strut) (ton)	Effective prestress (N/mm^2)
1000	140	30	983	34	562	688	8.6

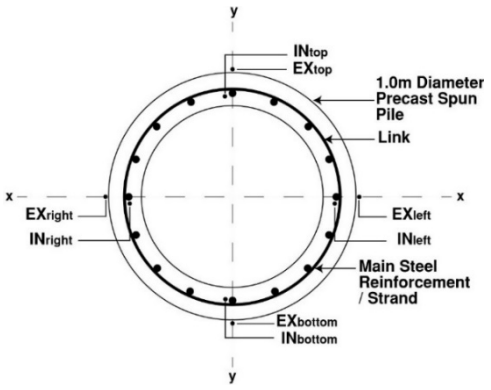

Fig. 3 Instrumentation layout of fibre optic cables in spun-cast pile, Type A embedded cables as "IN" and surface mounted Type B cables as "EX"

core. For the surface attachment sensing cable, it comprised of a 0.9-mm diameter optical cable with Hytrel® cable jacket similar to the inner fibre of NanZee reinforced cable (Lu *et al*. 2012).

The cable is also tight buffered so that the strain applied externally (from the concrete) is fully transferred to the inner core. The sensing cable can be mounted to concrete pile surface with epoxy. All the optical sensing cable used in this pile bending test was calibrated in laboratory by applying consistent strain increment to the sensing cable for up to ±15,000 $\mu\varepsilon$ and relates the quantity of strain changes to the quantity of frequencies shifted.

3. Preparation of test specimen

In order to integrate DOFSS measurements in the pile bending test, two precast spun piles of 30 m long, 1 m diameter were specially manufactured for the purpose of this study. The manufacturing plant and bending test site was in Lumut, Perak. Details of the pile specification are included in Table 1. Fig. 3 shows the general layout of optical fibre sensors with two pairs of strain sensing cables installed along the Prestressed Concrete Strand (PC) (Type A) and along the concrete surface (Type B). The cable positions were in accordance to 90° to each other so as to measure deformation in two axes (x-x & y-y) of the pile. Type A cables were loosely tied to the PC strand before casting so that the application of prestressing force prior to concreting was not transferred to the optical cables. Fig. 4 shows the installation of the sensing cables before and after curing was completed.

Upon the completion of curing process and the external surface of the pile was dried, four external Type B cables were fixed directly on the pile surface with the same alignment to the location of the cast-in cables with epoxy material to measure surface deformation. Accordingly, the surface attachment process was only performed when the pile had been lifted and secured on the loading frame. Since the pile specimens were very long, the bending tests were conducted in an outdoor environment (outside the fabrication yard). Once the surface gluing was completed, the epoxy was left for about two days to fully cure and was followed by the loading test programme the next day. These cables were connected through fusion splicing to form one complete loop of optical circuit for final connection to the BOTDA analyser.

4. Pile bending test procedures and measurement

Fig. 5 shows the pile bending test setup with loading and support configurations in accordance with Malaysian Standard MS 1314 Part 2: "Method for Determination of Bending Strength of Precast Concrete Piles". The standard specifies the requirement for supporting the test pile on two supporting rollers while the vertical load (hydraulic jack) is applied by two load-applying rollers. A load cell is fitted between the jack and the loading frame (for measurement of apply load) whereas five Linear Voltage Displacement Transducers (LVDTs) were used to measure the pile deflection across the span. For the test specimens, the test pile was set on a platform such that the top embedded optical cable (IN_{top}) lay directly below the load application rollers and aligned according to the vertical Y-Y axis. The Y-Y axis comprised of the bottom embedded cable marked as IN_{bottom} and a pair of surface cables (EX_{top} and EX_{bottom}). In the case of the later cables, it was necessary for the surface cables, EX_{top} and EX_{bottom} to shift the alignment slightly for the part below the load applying rollers and supporting rollers, respectively, in order to avoid fibre breakages. The horizontal axis, X-X (located at the neutral axis of the pile), comprised of a pair of embedded cables, IN_{left} and IN_{right} and surface cables, EX_{left} and EX_{right}. Only the internal fibres measured full length of the pile strain profile whereas the surface fibres measured strain section between the two supports.

According to MS 1314, there is no stipulation or provision for application of loading in cycles nor the necessity for recording of induced strain, although the standards specify the loading rate to be 0.06 ± 0.04 N/mm^2/s and monitored accordingly for compliance. In this study, three loading cycles were decided, the first two cycles comprising incremental loading to reach serviceability load, P_{ser} (here calculated to be 77 kN after excluding the concrete self-weight). In the final cycle, the test pile was loaded to an estimated cracking load of P_{cr} = 150 kN, in which the load was held temporarily to allow damage inspection. If cracks were present, the location,

width and length were recorded. The acceptance criterion for the test in accordance to the Malaysian Standard is deemed acceptable if the crack width at P_{cr} is less than 0.03 mm. The loading is then continued at the same specified rate until either failure occurs or when the applied load is slightly greater than the designed minimum ultimate load, $P_{min\text{-}u}$, whichever comes first. The minimum ultimate load ($P_{min\text{-}u}$) is a value corresponding to the value of crack moment, M_c multiplied by the factor stipulated in the Malaysian Standard. In the latter case, further load is added to reach the ultimate value, P_{ult} and the pile is inspected for cracking (e.g., crack width and length).

As mentioned previously, the BOTDA analyser was connected to the final two ends of optical fibre pigtails for the measurement of a full strain profile along the whole length of the pile. The BOTDA analyser was set with spatial resolution of 5 ns, which is equivalent to a convoluted gauge length of 50 cm. However, the reading trace can be plotted at every 5 cm along the cable's distance. Prior to the application of the load, a strain baseline reading was taken. Subsequent measurements were taken according to the pile bending test loading cycle schedule.

4.1 Temperature issue

As the 30-m long pile bending experiment required large space, the test rig could only be accommodated outside of the building. This posed a problem of maintaining constant temperature of the specimens as, under the outdoor environment, the pile might thermally expand or contract and affect the strain readings. In addition, temperature compensation of Brillouin based sensors are not that straightforward as it requires a composite thermal expansion coefficient of the optical cables inside the pre-stressed concrete (Mohamad *et al.* 2014). For example, in a free or loose fibre of Brillouin sensing, a change in 1°C will cause a shift in the strain of about 20 microstrain. In this study, the free loop section from surface mounted fibre (positioned at one end as shown in Fig. 5) was inferred to obtain the corresponding temperature of the concrete. During the first experiment of pile bending test (Pile No. 1), the effect of temperature in the strain measurements was significant with induced thermal strains of over 300 microstrain despite the outdoor temperature only rising to about 5°C (morning to noon). This means the surface temperature of the concrete increased to more than 15°C as opposed to the atmospheric temperature.

Rather than incorporating a complex temperature compensation procedure for concrete with pre-stressed tendons, an alternative approach was by minimising the effect of temperature fluctuation itself. In the next

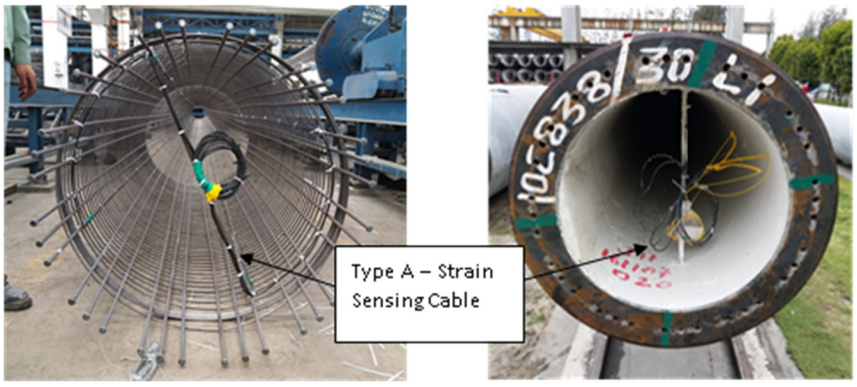

(a) Condition before casting (b) Condition after the pile after casting

Fig. 4 Attachment of optical cables along the PC strand

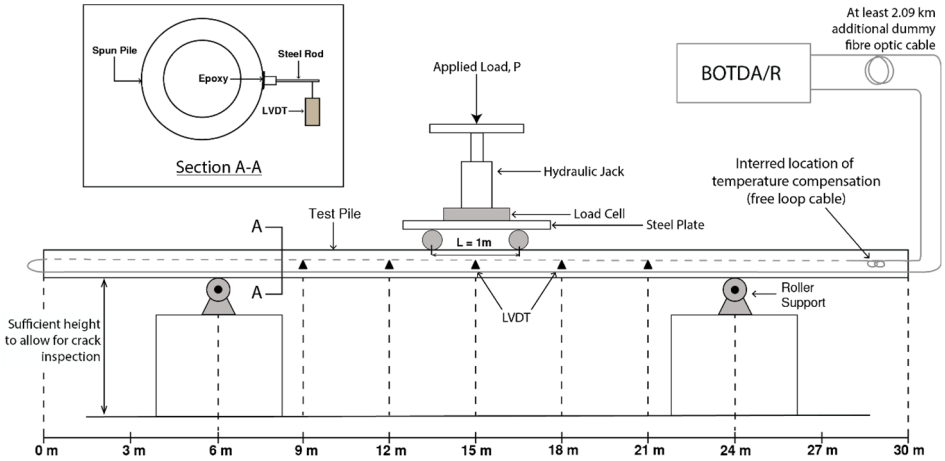

Fig. 5 Load bending test setup for precast-spun pile

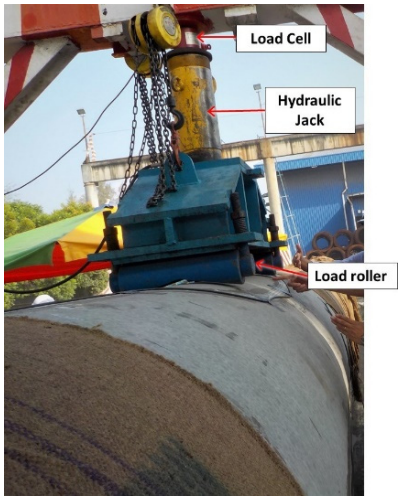

(a) Jacking system

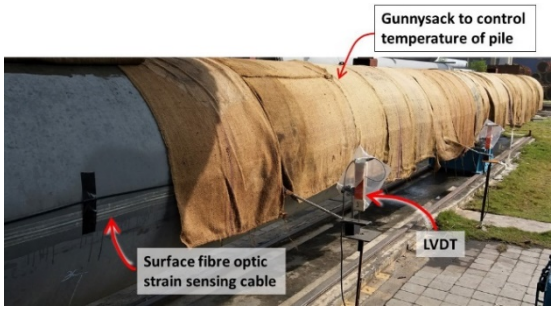

(b) Surface mounted optical fibres and LVDT

Fig. 6 Outdoor environment of load bending test

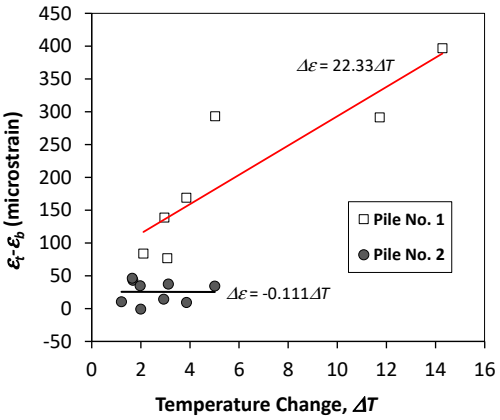

Fig. 7 Average bending strains recorded in the pile at distance of 27 m during service moment loadings

experiment (Pile No. 2), the specimen was shielded from direct sunlight by covering the pile with damp gunnysacks (see Fig. 6(b)). Based on the strain data obtained in the second load test, the effect of temperature was minimal.

As an example, Fig. 7 shows measurement of bending strains from the pair of embedded optical cables (top and bottom) measured at the pile distance of 27 m for both experiments. Assuming no prestress loss occurs in the steel tendons during "elastic" loading cycles, the curvature or bending moment outside the two roller supports is zero or free from bending strains. Unfortunately, it was not the case of Pile No. 1, as there was a linear correlation between strains and temperature. Conversely in the second test, the bending strains remained relatively constant and near zero. It was concluded that only the data from the second load bending test were used in the analysis.

4.2 Calculation of deflection

For simplicity, the pile longitudinal behaviour subjected to bending load can be represented by Euler-Bernoulli beam theory. Using the strain profile of two parallel sensing cables, the changes in the pile's curvature, q and transverse deformation, y along the distance, x of the pile can be calculated using the equations below

$$\varphi(x) = (\varepsilon_t - \varepsilon_b)/D \quad (1)$$

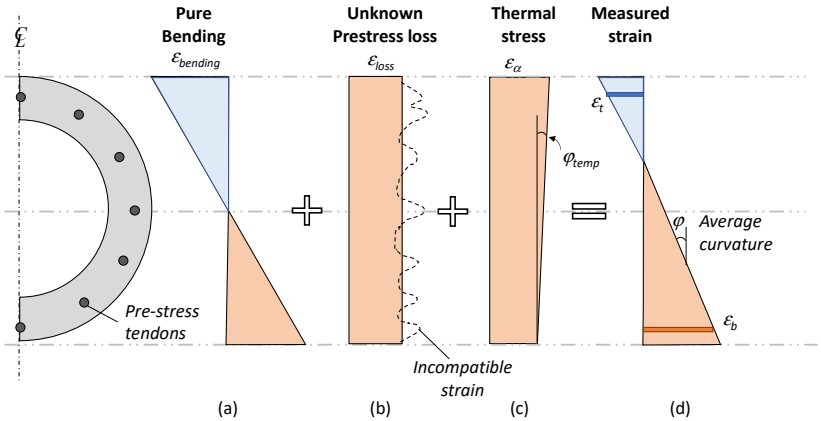

Fig. 8 Internal and external factors contributing to variation of strain measurements in the field

Where
j is curvature or bending strain
ε_t and ε_b are strain measurement at two opposite fibres (top and bottom),
D is distance between the two fibres or diameter of pile

$$y(x) = \iint \varphi dx + C_1(x) + C_2 \quad (2)$$

A polynomial function is fitted in Eq. (1) data so that the integration process in Eq. (2) can be done analytically. This is by applying suitable boundary conditions, such as zero displacements, at the two beam supports. The relationship between curvature and bending moment, M, is shown below

$$\varphi(x) = M/EI \quad (3)$$

Where
EI is flexural stiffness of the pile

For axially loaded piles with bending deformation (as in many field applications), Eq. (1) is still valid provided that axial stresses or strains within the two sides of the piles are equally distributed. The axial deformation, z along the pile with known displacement at the head or toe can be calculated as below

$$z(x) = \int \frac{\varepsilon_t + \varepsilon_b}{2} dx + C_3 \quad (4)$$

4.3 Data interpretation of bending strains

In principle, deflection of an ordinary axisymmetric beam under pure bending during elastic loading yields equally distributed compression and tension stresses across the beam's neutral axis (Fig. 8(a)). In this study however, the longitudinal strains measured from the two opposite sides of optical fibres may not necessarily resulted in equal amount of compressive and tension regions (Fig. 8(d)). For the prestressed concrete member, factors such as prestress loss from the pretensioned tendons, tendon slippage and thermal effect should be considered when interpreting strain data from the optical fibres. Measurement of prestressing losses is difficult because it requires that concrete strain be determined from the time when the prestress is transferred until the end of the measurement period (e.g., Kim *et al.* 2015). Under additional loads, the prestress reinforcement (at the soffit) can elongate and cause an increase in effective prestress force. This increase is effectively a partial recovery of prestress loss that is sometimes called elastic gain (see ACI 423.10R-16, Guide to Estimating Prestress Loss). On the compression side, elastic shortening loss can occur as the result of the prestress reinforcement having to contract and cause a reduction in effective prestress force. The magnitude of the elastic shortening loss is not uniform along the pretensioned member. For a pile under flexure beyond the limit of tendon stress, some slip of the tendon occurs (Fig. 8(b)). At this point, the strains from the tendons may not be compatible with the adjacent concrete. The variation in stress limit in a prestressing steel tendon depends on several variables. Among them are the stress in the tendon due to initial prestress, the maximum possible

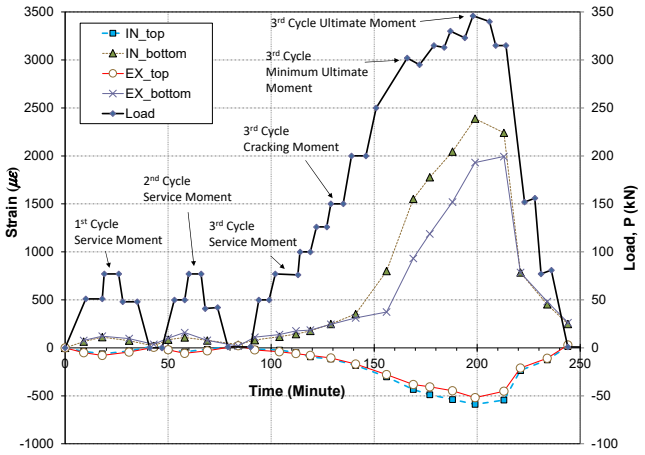

Fig. 9 Time series of loading with comparison of bending strains at mid-span recorded between internal and external sensors

stress in the tendon at the flexural strength, and the load transfer length of the tendon (Joen and Park 1990).

As the experiment of load bending test was conducted in the outdoor environment, temperature variation (due to ray of sunlight) can cause non-uniform thermal expansion across the structural element. The thermal effects are considered to cause tensile strain as shown in Fig. 8(c). As mentioned earlier, compensating for the thermal effects from each sensing fibre is a lengthy process. The method requires temperature cables to be installed side by side along the strain sensing cables and inferring the thermal strain changes at every cross-section of the pile. Fortunately, removing the thermal effects from BOTDA reading may not be necessary if the primary objective of the experiment is to monitor the flexural performance of the pile. If the temperature profile at any cross-section of. the. pile is equal. between. top. and. bottom (meaning no thermal gradient, φ_{Temp} = 0), the thermal expansion components are self-cancelled when calculating the curvature changes (Eq. (1)). The curvature profile is not affected by variation of temperature between the left and right supports so long as φ_{Temp} is kept to zero. The method of applying damp cloths in controlling the temperature gradient was successful as shown earlier in Fig. 7. In the case of Pile No. 2, φ_{Temp} was only 0.138 $\mu\varepsilon$ /m/°C. This thermal gradient can be considered negligible when characterising bending behaviour of prestressed concrete pile (see later in Fig. 22).

5. Measurement results

5.1 Comparison between internal and external fibres

Fig. 9 shows the evolution of bending strains of all cables taken at the mid-span of the pile during the three cycles of load bending test. Under the service moment, in general, all the four sensors located at the top and bottom of the pile performed similarly between internal and external fibres. There were consistent strains increment

(compression and tension) from all internal and external sensing cables upon reaching the first design cracking moment, here when P_{cr} = 150 kN. Beyond this elastic loading, the distribution of bending strains between internal and external sensors began to deviate, in particular the tensile region compared to the compression side. For example, during the application of ultimate load, P_{ult} = 345 kN, the embedded sensor recorded tensile strain of +2388 $\mu\varepsilon$ compared to +1931 $\mu\varepsilon$ by the surface fibre (a difference of 450 $\mu\varepsilon$). In the case of compression side, the internal fibre recorded -589 $\mu\varepsilon$, 70 $\mu\varepsilon$ higher (in compression) than the external fibre. The Euler-Bernoulli beam theory may not be applicable for this specimen, as the outermost fibres of the same plane (in this case, the external top and bottom fibres) did not record the highest strain as opposed to the internal fibres (see also later Fig. 16). When considering the position of the fibres, it is likely that the internal fibres measure strains which are compatible to the strains of pre-tensioned wires.

Figs. 10 and 11 present the corresponding load versus strains of the midspan, which further illustrate the elastic behaviour of the pile under service load. The pile returned to the original position after two loading cycles and deformed consistently in linear upon reaching to the limiting design cracking load, P_{cr}. Broadly speaking, there was no plastic deformation in the compression side of the pile even after the application of ultimate load. However, in the tension side of the pile, plastic/residual strains of about 250 $\mu\varepsilon$ were recorded by both type of fibres. Under the service load, tensile strain was almost double the amount in compression when measured using internal fibre whereas the surface fibre recorded tensile strain 40% higher than in compression. It can be observed during the application of maximum load, the ratio of tensile to compressive strains in both the internal and surface fibre increased to about four times. This observation may be attributed to the variation in stress limit in a prestressing steel tendon, (see earlier discussion in Sec. 4.3).

A sample of bending strain distributions taken during the application of service moment from the first cycle is shown in Fig. 12. Although the shape of strain profiles between tension and compression were broadly symmetrical, the magnitude of the strains was different. The two fibres located at the soffit recorded maximum bending strains of about +100 $\mu\varepsilon$ whereas the top fibres generally recorded mid-span compressive strains of about -50 $\mu\varepsilon$. As for the fibres in the neutral axis of the beam, there was a slight tension of about +23 $\mu\varepsilon$. The inequality of strains between opposing fibres were likely due to the thermal effect which was not compensated from the strain measurements (error from thermal strain fluctuation estimated to be around 25 to 50 $\mu\varepsilon$ based on Fig. 7).

Figs. 13 to 15 further compare the development of compressive and tensile strains of the pile recorded from all sensing cables. In Fig. 13 where the load is at the first designated cracking moment, the internal and external fibres performed almost similarly with maximum tensile strain recorded as 250 $\mu\varepsilon$ and -100 $\mu\varepsilon$ in the compression.

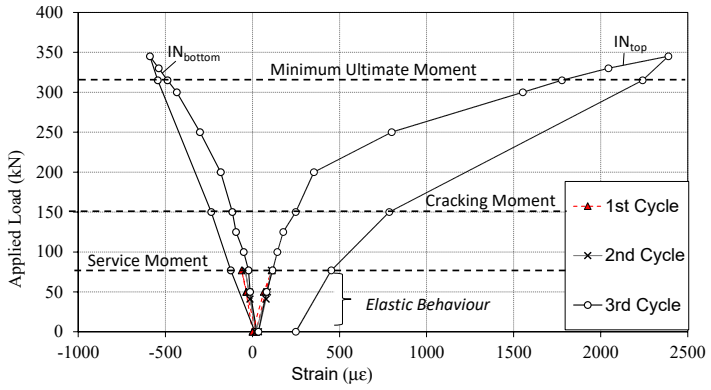

Fig. 10 Load vs. Strain for embedded sensing cables measured at mid-span of pile

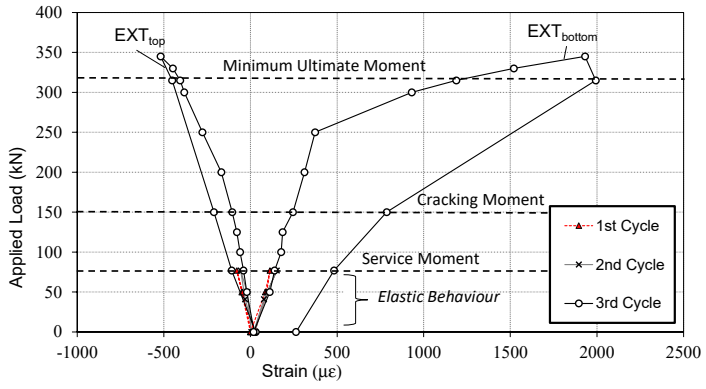

Fig. 11 Load vs. Strain for surface sensing cables measured at mid-span of pile

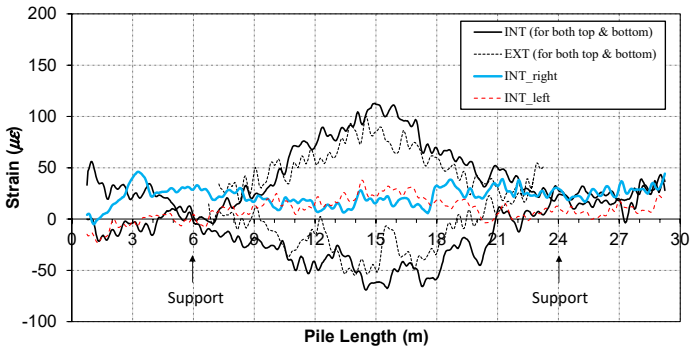

Fig. 12 Load vs Strain of all sensing cables under working load condition, P = 77 kN

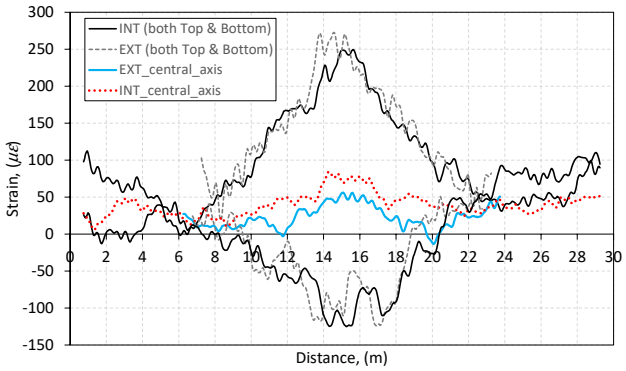

Fig. 13 Load vs Strain of all sensing cables under working load condition, P_{cr} = 150 kN

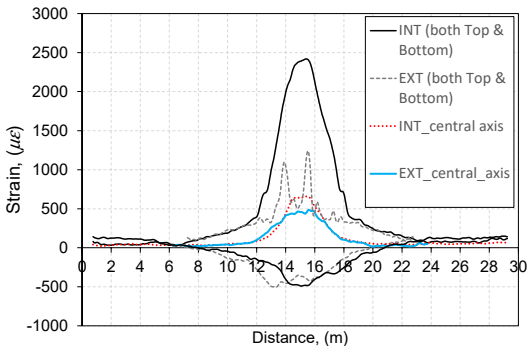

Fig. 14 Load vs Strain of all sensing cables under ultimate load, $P_{min\text{-}u}$ = 315 kN

In contrast, Figs. 14 and 15, where the load had reached twice the working load and beyond, show the maximum tensile strains profile between the embedded and surface bonded cables differed remarkably. The internal fibre recorded maximum tensile strain of 2380 $\mu\varepsilon$ but the surface sensors showed irregular strain peaks or spikes near the loading points. These spikes were attributed to the development of tensile cracks at the soffit, but the magnitude was much less than the one from the embedded fibre. At the central axis of the pile, tensile strain increased from zero at the support to about 500 $\mu\varepsilon$ at the midspan after reaching minimum ultimate load of $P_{min\text{-}u}$ = 315 kN (Fig. 14).

Fig. 16 shows the distribution of bending strain at the midspan of pile (9 m from the support) under the selected loading stages. For measurements at the centre of the beam (neutral plane), the strains were averaged from four different sets of cables (see Fig. 3). At the beginning of the service load, the averaged strains at the centreline of the pile axis are not zero (slight tension of about +23 $\mu\varepsilon$). This is likely because of the thermal effect which was not compensated as previously discussed in Fig. 12. As the pile flexes down due to the increasing vertical loading, the pile neutral axis shifts upward (230 mm from the centreline), corresponding to stiffness reduction in the reinforced concrete member when tensile cracks were present. Similar observation (the neutral axis moved upwards with the propagation of cracks) was reported by Ni *et al.* (2017). A model of the beam cracking in Fig. 17 matches the observed data presented in Fig. 16. The stiffness of the cracked concrete section, in which there was no tensile resistance of concrete, was much lower than that of the uncracked gross section. However, tension stiffening effect provided by the bond between concrete and steel in-between the cracks enhanced the average member stiffness above the cracked section stiffness (Vitharana 1997). Hence, the surface bonded fibre recorded lower strains between the cracks as compared to the embedded fibre, in which the latter experienced much higher tensile strains due to the attachment with the steel strand.

5.2 Cracks observation

Fig. 18 presents the crack line mapping at the soffit of 19 individual cracks, all of which occurred within 3 m away from the mid span of the pile (zone approximate 1/3 of supported pile length). The first crack, labelled as "1A" appeared right after the load exceeded the Design Cracking

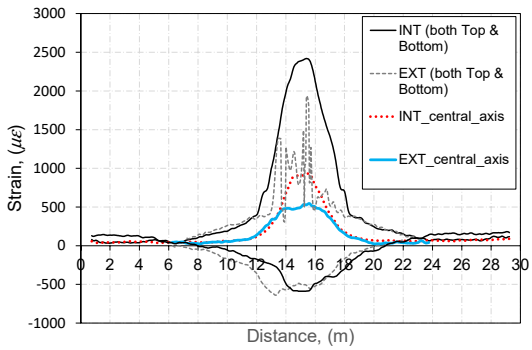

Fig. 15 Load vs Strain of all sensing cables under maximum load, P_{ult} = 345 kN

Moment, P_c = 155 kN (crack width < 0.05 mm). At the maximum applied load of P_{ult} = 345 kN, this crack grew to about 0.35 mm (the largest crack) and corresponded exactly to the peak strain of 1931 $\mu\varepsilon$ measured by the surface fibre at the soffit (see Fig. 15). To further compare the surface strain at the soffit with the observed cracks, Fig. 19 illustrates the colour tone of optical fibre strains at every loading step of the third cycle. The figure is superimposed with the crack lines recorded during the final loading step. As can be seen, the strain with the red contour (strain of over 1500 $\mu\varepsilon$) only appeared after the load reach 250 kN and located between 13 m and 17 m of the span. Beyond this range, the section of the pile may still behave elastically even after reaching the ultimate load. This is related to the bending stiffness of the pile, which is described in the next section.

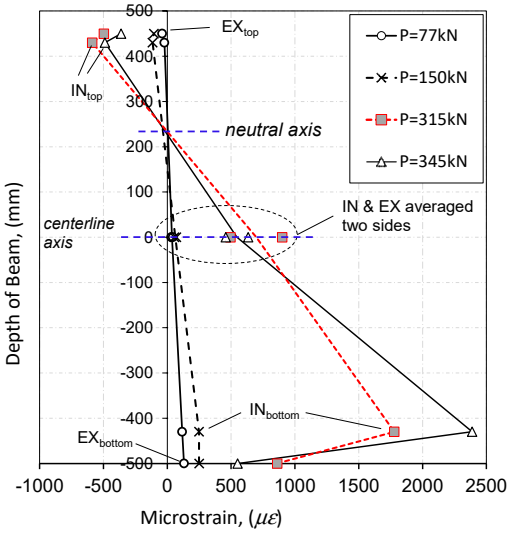

Fig. 16 Strain distribution along the vertical cross-section of PHC pile

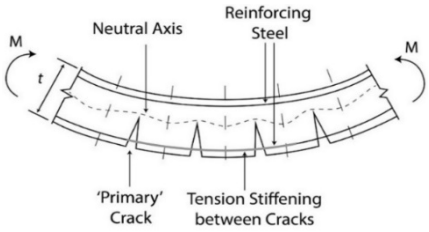

Fig. 17 Tension stiffening mechanism (after Vitharana 1997)

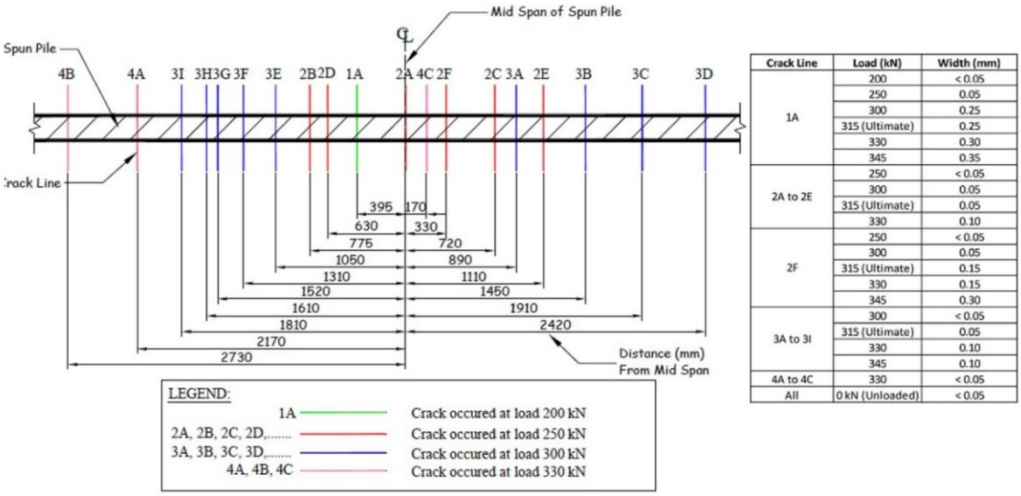

Crack Line	Load (kN)	Width (mm)
1A	200	< 0.05
	250	0.05
	300	0.25
	315 (Ultimate)	0.25
	330	0.30
	345	0.35
2A to 2E	250	< 0.05
	300	0.05
	315 (Ultimate)	0.05
	330	0.10
2F	250	< 0.05
	300	0.05
	315 (Ultimate)	0.15
	330	0.15
	345	0.30
3A to 3I	300	< 0.05
	315 (Ultimate)	0.05
	330	0.10
	345	0.10
4A to 4C	330	< 0.05
All	0 kN (Unloaded)	< 0.05

Fig. 18 Crack line mapping at soffit of pile

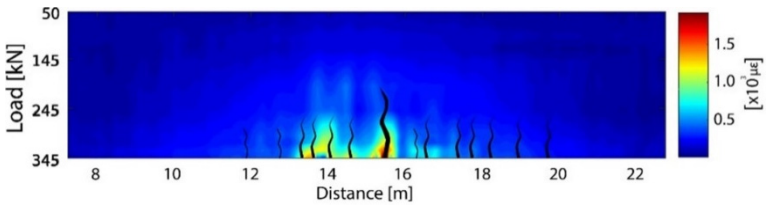

Fig. 19 Interpolated surface strain increment at soffit by optical fibre and the corresponding crack map at load of 345 kN

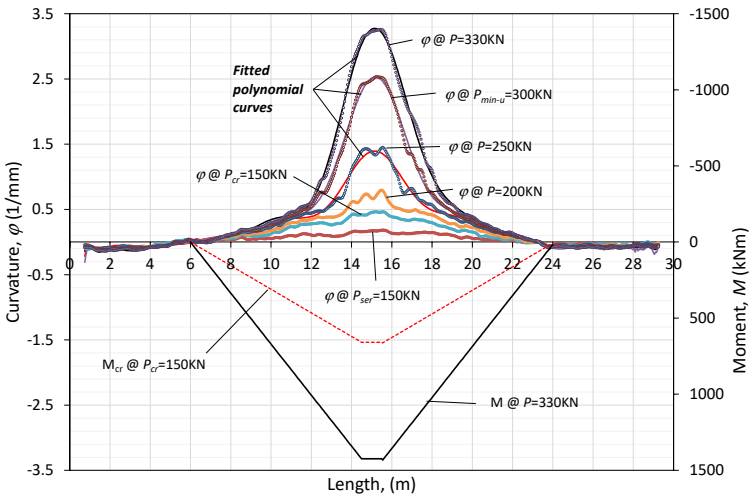

Fig. 20 Curvature profile of PHC spun pile during third cycle loading stage

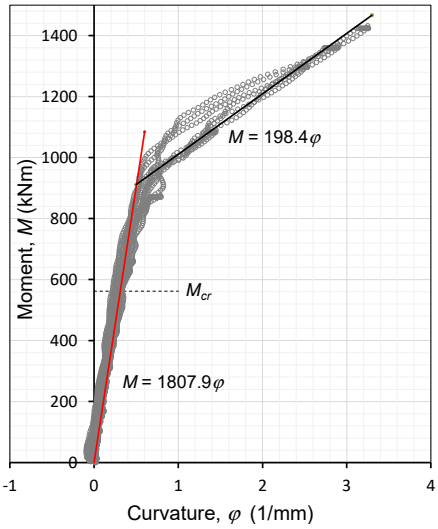

Fig. 21 Moment-curvature response of PHC spun pile

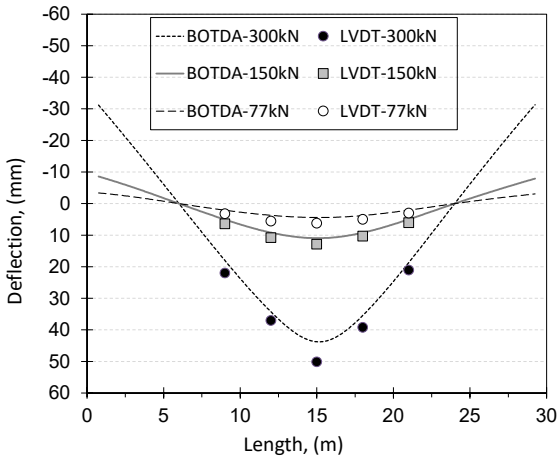

Fig. 22 Beam deflection measured by optical fibres and LVDTs at critical loading stages

5.3 Bending moment vs. curvature

The stiffness degradation with the onset of cracking is significant and rapidly varies with the flexural moment. Fig. 20 shows the curvature changes calculated from the bending strains of sensing cables embedded in the top and bottom of PHC pile (see Eq. (1)). Examples of induced bending moment curves calculated based on Euler-Bernoulli beam principle or elastic theory are also plotted in Fig. 21. The bending moment increases linearly from the roller supports going towards the point load and maintains constant in-between the two-point loads. Similar profile is expected from curvature profile (from optical fibres). However, when the applied load exceeds the elastic limit, the curvature profile increases rapidly in comparison to the induced bending moment.

Distributed optical fibre sensor has the advantage of measuring the effective moment-curvature relationship along the whole length of a structural element. Using the data provided in Fig. 20, the pile's moment-curvature relationship (Eq. (3)) is plotted in Fig. 21. In this case, the non-linear behaviour occurred way after the specified yield moment or the pile's design moment capacity of M_{cr} = 562 kNm. Interestingly, the curve can be presented by two linear fits of bending stiffnesses, the elastic stiffness of EI = 1808 MNm^2, which matches bending moment up to 850 kNm, and the yielded flexural stiffness, EI_{crack} = 198 MNm^2, when the moment exceeds 900 kNm. In this experiment, cracking at the soffit causes the flexural rigidity of PHC pile to reduce by 89%. The pile did not fail even reaching design ultimate load, M_{ult} = 1300 kNm. Under the serviceability load, the calculated Young's modulus of this PHC pile is 50 kN/mm^2.

5.4 Derivation of deflection profile from BOTDA

High-order polynomial curves were fitted into the curvature plots, as exemplified in Fig. 19. The curve fitting was performed using MATLAB® function called *Polyfit* that computes a least squares polynomial for a given set of data and generates suitable coefficients of the polynomial. In this study, a 27th order was used, which was sufficiently accurate to model the curvature data (a higher number

would not improve the accuracy significantly). By applying Eq. (2), the polynomial functions can be integrated twice to obtain the deflection profile and referring to displacements recorded by LVDT at positions 9 m and 21 m.

Fig. 21 compares the results of deflection by optical fibres (integrated curvature profile) and the measured displacements from five LVDTs. As can be seen, there is excellent agreement between the bending displacements between the two systems. Only at the maximum load of 300 kN, the maximum deflection recorded by LVDT is slightly higher at 50 mm as compared to 47 mm by BOTDA.

6. Conclusions

The flexural behaviour of PHC spun pile from the field bending test was well-described using distributed optical fibre strain sensor. The pile exhibited more tension stresses under bending with neutral plane (zero strain) appeared on the upper side above the central axis. The internal fibres recorded strains much higher than external fibres, particularly under high load. The experimental results indicated the bending strength of the pile was above the manufacturer's design. No cracks (or crack width > 0.03 mm) were observed during loading stage of P_{cr} = 150 kN, meaning the pile achieved the bending strength as stipulated by the Malaysian Standard. The tensile cracks observed on the pile matched with the strain spikes recorded by the surface mounted fibre at the soffit. The tensile strains between the cracks were much lower than the ones recorded by the embedded fibre, indicating the tension stiffening effect due to the nature of stress interaction between concrete and the PC strand. When compared with moment-curvature response, the flexural rigidity curve can be modelled using simple bilinear parameters. This information is useful for pile designers whenever determining the serviceability and ultimate loads imposed to the structure. It is expected in the future that more precast product, such as spun-cast piles, will be integrated with optical fibre sensors where the data can be inferred as part of advanced structural health monitoring scheme.

References

Abendroth, R.E., Greimann, L.F. and LaViolett, M.D. (2007), "An Integral Abutment Bridge with Precast Concrete Piles", IHRB Project TR-438, Iowa Highway Research Board & Iowa Department of Transportation, USA.

Abu-Farsakh, M.Y., Haque, M.N. and Tsai, C. (2017), "A full-scale field study for performance evaluation of axially loaded large-diameter cylinder piles with pipe piles and PSC piles", *Acta Geotech*., **12**(4), 753-772. https://doi.org/10.1007/s11440-016-0498-9

Aso, T., Miura, F., Inoue, T. and Yamamoto, M. (2004), "Non-linear bending characteristics of PHC piles under varying axial load", *Proceedings of the 13th World Conference on Earthquake Engineering*, WCEE, in CD-ROM, 1-9.

Avent, R.R. and Mukai, D.J. (1998), "Investigation of Cracks in Cylindrical Spun-Cast Concrete Piles in a Marine Environment", Louisiana Transportation Research Center, LA-98/320.

Bao, Y., Tang, F., Chen, Y., Meng, W., Huang, Y. and Chen, G. (2016), "Concrete pavement monitoring with PPP-BOTDA distributed strain and crack sensors", *Smart Struct. Syst*., *Int. J*., **18**(3), 405-423. http://doi.org/10.12989/sss.2016.18.3.405

Chow, C.C. and Tan, Y.C. (2010), "Performance of jack-in pile foundation in weathered granite", *Proceedings of the 17th SEA Geotechnical Conference*, Taipei, Taiwan, pp. 1-4.

Feng, X., Wu, W., Li, X., Zhang, X. and Zhou, J. (2015), "Experimental investigations on detecting lateral buckling for subsea pipelines with distributed fiber optic sensors", *Smart Struct. Syst*., *Int. J*., **15**(2), 245-258. http://doi.org/10.12989/sss.2015.15.2.245

Goldfeld, Y. and Klar, A. (2013), "Damage identification in reinforced concrete beams using spatially distributed strain measurements", *J. Struct. Eng*., **139**(12), 04013013. https://doi.org/10.1061/(ASCE)ST.1943-541X.0000795

Hartman, J.J., Castelli, R.J. and Malhotra, S. (2007), "Design and Installation of Concrete Cylinder Piles", In: *Contemporary Issues in Deep Foundations*, (in W. Camp, R. Castelli, D.F. Laefer and S. Paikowsky eds.), American Society of Civil Engineers.

Hong, W.P., Kim, J.H. and Hong, S. (2019), "Role of piles in mitigating the movement of pipes in soft grounds during embankment loading", *Mar. Georesources Geotechnol*., **37**(9), 1019-1031. https://doi.org/10.1080/1064119X.2018.1523973

Huang, X., Yang, M., Feng, L., Gu, H., Su, H., Cui, X. and Cao, W. (2017), "Crack detection study for hydraulic concrete using PPP-BOTDA", *Smart Struct. Syst*., *Int. J*., **20**(1), 75-83. https://doi.org/10.12989/sss.2017.20.1.075

Joen, P.H. and Park, R. (1990), "Flexural strength and ductility analysis of spirally reinforced prestressed concrete piles", *PCI J*., **35**(4), 64-83. https://doi.org/10.15554/pcij.07011990.54.83

Joint ACI-ASCE Committee 423 (2016), ACI PRC-423.10-16 Guide to Estimating Prestress Losses, American Concrete Institute, Farmington Hills, MI, USA.

Kesavan, K., Ravisankar, K., Parivallal, S. and Sreeshylam, P. (2005), "Applications of fiber optic sensors for structural health monitoring", *Smart Struct. Syst*., *Int. J*., **1**(4), 355-368. https://doi.org/10.12989/sss.2005.1.4.355

Kim, S.T., Park, Y., Park, S.Y., Cho, K. and Cho, J.R. (2015), "A sensor-type PC strand with an embedded FBG sensor for monitoring prestress forces", *Sensors*, **15**(1), 1060-1070. https://doi.org/10.3390/s150101060

Liew, S.S., Lee, S.T. and Koo, K.S. (2010), "Failure Investigation of Piled Reinforcement Soil Wall & Excessive Movements of Piled Embankment at Soft Ground, Malaysia", *Proceedings of the 17th Southeast Asian Geotechnical Conference*, Taipei, Taiwan, 3P-191.

Liu, H.B., Zhang, Q. and Zhang, B.H. (2017), "Structural health monitoring of a newly built high-piled wharf in a harbor with fiber Bragg grating sensor technology: design and deployment", *Smart Struct. Syst*., *Int. J*., **20**(2), 163-173. https://doi.org/10.12989/sss.2017.20.2.163

Lu, Y., Shi, B., Wei, G.Q., Chen, S.E. and Zhang, D. (2012), "Application of a distributed optical fiber sensing technique in monitoring the stress of precast piles", *Smart Mater. Struct*., **21**(11), 115011. https://doi.org/10.1088/0964-1726/21/11/115011

Mohamad, H., Soga, K. and Amatya, B. (2014), "Thermal strain sensing of concrete piles using Brillouin optical time domain reflectometry", *Geotech. Test. J*., **37**(2), ASTM, 333-346. https://doi.org/10.1520/GTJ20120176

Mohamad, H., Tee, B.P., Ang, K.A. and Chong, M.F. (2016), "Characterizing anomalies in distributed strain measurements of cast-in-situ bored piles", *Jurnal Teknologi*, **78**(8-5), 75-82. https://doi.org/10.11113/jt.v78.9626

Mohamad, H., Tee, B.P., Chong, M.F. and Ang, K.A. (2017), "Investigation of shaft friction mechanisms of bored piles

through distributed optical fibre strain sensing", *Proceedings of the 19th International Conference on Soil Mechanics and Geotechnical Engineering*, ISMGE, pp. 2829-2832.

Mohamad, H., Tee, B.P., Chong, M.F., Ang, K.A., Rashid, A.S.A. and Abdullah, R.A. (2019), "Instrumented laterally loaded pile test using distributed fibre optic sensor", *Geotech. Eng.*, **50**(2), 36-42.

MS1314: Part 2 (2004), Precast Concrete Piles: Part 2: Method for Determination of Bending Strength of Precast Concrete Piles (Bend Test), Malaysian Standard, Department of Standards Malaysia.

Ni, P., Mangalathu, S., Mei, G. and Zhao, Y. (2017), "Compressive and flexural behaviour of reinforced concrete permeable piles", *Eng. Struct.*, **147**, 316-327. https://doi.org/10.1016/j.engstruct.2017.06.007

Pelecanos, L., Soga, K., Elshafie, M.Z.E.B., Battista, N., Kechavarzi, C., Gue, C.Y., Ouyang, Y. and Seo, H.J. (2018), "Distributed fiber optic sensing of axially loaded bored piles", *J. Geotech. Geoenviron. Eng.*, **144**(3), 04017122. https://doi.org/10.1061/(ASCE)GT.1943-5606.0001843

Rausche, F. and Webster, S. (2007), "Behavior of cylinder piles during pile installation", In: *Contemporary Issues in Deep Foundations*, (in W. Camp, R. Castelli, D.F. Laefer and S. Paikowsky eds.), American Society of Civil Engineers.

Vitharana, N. (1997), "Rational prediction of lateral behaviour of concrete piles incorporating pile (concrete) non-linearity", *Proceedings of the 14th International Conference on Soil Mechanics and Foundation Engineering*, Recent developments in foundation techniques, pp. 915-920.

Völgyi, I., Farkas, G. and Nehme, S.G. (2010), "Concrete strength tendency in the wall of cylindrical spun-cast concrete elements", *Period Polytech.-Civil*, **54**(1), 23-30. http://dx.doi.org/10.3311/pp.ci.2010-1.03

Whiting, W.A. (1952), "Reinforced concrete pipe", U.S. Patent, No. 2,602,469, 8 Jul. 1952.

Zou, L., Bao, X., Yang, S., Chen, L. and Ravet, F. (2006), "Effect of Brillouin slow light on distributed Brillouin fiber sensors", *Opt. Lett.*, **31**(18), 2698-2700. http://dx.doi.org/10.1364/OL.31.002698

HJ